Correlating planar microstructures in shocked zircon from the Vredefort Dome at multiple scales: Crystallographic modeling, external & internal imaging, and EBSD structural analysis

REVISION 1

Timmons M. Erickson[1,]*, Aaron J. Cavosie[1], Desmond E. Moser[2], Ivan R. Barker[2], and Henri A. Radovan[3]

1. Dept. of Geology, University of Puerto Rico Mayagüez, P.O. Box 9000, Mayagüez, Puerto Rico, 00681-9000 U.S.A. *Corresponding Author: Timmons.Erickson@gmail.com

2. Dept. of Earth Sciences, Western University, London, ON, N6A 5B7, Canada

3. Dept. of Physics, University of Puerto Rico Mayagüez, P.O. Box 9000, Mayagüez, Puerto Rico, 00681-9000, U.S.A.

Keywords: Shock metamorphism, zircon, Vredefort Dome, planar fractures

Abstract

Microstructural and geochronological analysis of shocked zircon has greatly advanced understanding the formation and evolution of impact structures. However, fundamental aspects of shock-produced planar microstructures in zircon remain poorly known, such as their deformation mechanisms, crystallographic orientations, and how planar microstructures visible at the grain scale by scanning electron microscopy correlate to microstructures visible at sub-μm scales by transmission electron microscopy and electron backscatter diffraction (EBSD). In order to unify observations of planar microstructures in zircon made at different scales into a consistent framework, we integrate the results of (1) three dimensional crystallographic modeling of planar microstructure orientations, with (2) 360° external prism backscattered electron imaging at the grain scale, and (3) polished section cathodoluminescence and EBSD analysis at the sub-μm scale for a suite of detrital shocked zircons eroded from the Vredefort Dome in South Africa. Our combined approach resulted in the documentation of seven planar microstructure orientations that can be correlated from grain to sub-μm scales of observation: (010), (100), (112), $(1\bar{1}2)$, $(\bar{1}12)$, $(\bar{1}\bar{1}2)$ and (011). All orientations of planar microstructures exhibit minor variations in style, however all are considered to be fractures; no amorphous $ZrSiO_4$ lamellae were identified. We therefore favor the usage of 'planar fracture' (PF) over 'planar deformation feature' (PDF) for describing the observed planar microstructures in zircon based broadly on the nomenclature developed for shocked quartz. Some {112} PFs visible at the grain scale contain impact microtwins detectable by EBSD, and are the first report of polysynthetic twinning in zircon. The microtwins consist of parallel sets of thin lamellae of zircon oriented 65˚ about <110> and occur in multiple cross-cutting {112} orientations within single grains. Curviplanar fractures and injected melt are additional impact-related microstructures associated with PF formation. Crosscutting relations of shock microstructures reveal the following chronology: 1) Early development of c-axis parallel PFs in (010) and (100) orientations; 2) The development of up to four {112} PFs, including some with microtwins; 3) The development of curviplanar fractures and the injection of impact derived melt; 4) The development of (011) PFs associated with compressional deformation; and 5) Grain-scale non-discrete crystal plastic deformation. Experimental constraints for the onset of PFs, together with the absence of reidite, suggest formation conditions from 20 to 40 GPa for all of the planar microstructures described here.

Introduction

Meteorite impacts create unique microstructural deformation within minerals as a result of shock metamorphism, producing what are commonly referred to as shocked minerals (Stöffler and Langenhorst 1994; French 1998). The presence of shocked minerals within a suspected impact structure is now considered one of two diagnostic criteria necessary to confirm an impact origin (French and Koeberl 2010). Some types of shocked zircon can be used to date impact events (e.g. Krogh et al. 1993), and can encapsulate partial melts of the crater floor as glass inclusions (Moser et al. 2011). Shock microstructures in detrital zircons have recently been shown to survive post-impact thermal conditions, uplift, erosion and sedimentary transport, thus preserving a lasting record of impact processes in siliciclastic sediments (Cavosie et al. 2010; Erickson et al. 2011). Information from detrital and bedrock shocked zircon populations can thus be used to study a variety of impact processes. Shock microstructures in zircon are typically identified using scanning electron microscopy (SEM) imaging. As shock microstructures occur in numerous crystallographic orientations, which may relate to different crater environments, a better understanding of how planar microstructures visible on grain surfaces correlate to microstructures visible in polished section is needed. Despite recent advances in the microstructural analysis of shocked zircons by electron backscatter diffraction (EBSD), determination of the true crystallographic orientation of planar microstructures by EBSD is sometimes not possible either because the microstructure is a non-diffracting material (i.e. an open fracture) or because of non-unique three dimensional solutions resulting from data collected on a two dimensional polished sample. Here we combine modeling and detailed three dimensional imaging of shocked grains, together with cathodoluminescence (CL) and EBSD data from a suite of detrital grains from the Vredefort Dome impact basin in South Africa to better characterize impact-generated planar microstructures in zircon.

Shock microstructures in zircon have been observed in natural samples and in experimentally shocked grains. Krogh et al. (1984) first reported shock microstructures in zircon from the Sudbury

This is a preprint, the final version is subject to change, of the American Mineralogist (MSA)
Cite as Authors (Year) Title. American Mineralogist, in press.
(DOI will not work until issue is live.) DOI: http://dx.doi.org/10.2138/am.2013.4165

Basin, which contained sets of planar microstructures visible on grain surfaces. Bohor et al. (1993) described similar shock microstructures in zircon from different impact environments, including bedrock and ejecta. Leroux et al. (1999) experimentally shocked zircons cut perpendicular to their c-axes and analyzed the resulting planar microstructures with transmission electron microscopy (TEM). Planar microstructures in the experimentally shocked grains began to develop at 20 GPa through a progressive process involving microcracking and dislocation glide (Leroux et al. 1999). Reidite, a high pressure polymorph of zircon with scheelite structure, was found intergrown with zircon in samples shocked to 40 GPa, with complete transformation to reidite by 60 GPa (Leroux et al. 1999). Scheelite-type $ZrSiO_4$ was first reported by Reid and Ringwood (1969), and later proposed as a high-P polymorph of shock metamorphosed zircon (Kusaba et al. 1985). Naturally occurring reidite has since been reported in shocked zircons from both ejecta (Glass and Liu 2001; Glass et al. 2002) and suevite (Wittmann et al. 2006). Using TEM, Leroux et al. (1999) identified reidite forming along (100) in zircon and that $(100)_{zircon}$ corresponds to $(112)_{reidite}$. Twins were documented along $(112)_{reidite}$ planes within the shock produced reidite, but not within the host zircon. Gucsik et al. (2002) imaged the experimentally shocked zircons of Leroux et al. (1999) with cathodoluminescence (CL), but were unable to reproduce with CL the microstructures visible by TEM.

Granular zircon has also been reported from a variety of impact structures, where zircon re-crystalizes into equant neoblasts while still retaining the original morphology of the grain (Krogh et al. 1984; Bohor et al. 1993). Granular zircon has been used to determine the age of impact structures (e.g. Kamo et al. 1996; Moser 1997). At higher impact pressures and temperatures zircon converts to ZrO_2 and SiO_2 as reported by El Goresy (1965) in tektites. Kusaba et al. (1985) found that tetragonal ZrO_2 formed in experiments above 1775˚ C and 70 GPa, and it has been identified on the surfaces of shocked zircons in impact melt rocks at the Ries and Chicxulub impact structures (Wittmann et al. 2006).

Electron backscatter diffraction has been used to describe zircon plasticity (Reddy et al. 2007; Moser et al. 2009), shock microstructures (Nemchin et al. 2009; Moser et al. 2011; Timms et al. 2012), and to quantify the orientation of crystal domains at the surface of highly polished sections at sub-μm scale by indexing the patterns formed by electrons diffracting through the target crystal lattice. With EBSD, crystallographic misorientations of >0.5˚ within a grain can be identified. Several studies have used EBSD to gain new insights into the nature of shock deformation in zircon. Moser et al. (2009) used EBSD to document an apparent intra-grain shear zone within zircon from the Lace kimberlite near the Vredefort Dome, and attributed the microstructure to mantle flow caused by the Vredefort impact; the authors correlated the observed microstructural distortion to Pb loss at the time of the Vredefort impact event. Nemchin et al. (2009) identified low angle, sub-parallel grain boundaries within zircon from a lunar sample by EBSD. Moser et al. (2011) used EBSD to document that some planar fractures (PFs) in {1k2} orientation in zircon contain 1 to 2 μm wide lamellae of zircon with an apparent rotation of 65˚ about <110>. The authors also identified glass inclusions of partial melt derived from the host rock, and a five-step sequence of shock microstructure development (Moser et al. 2011). Timms et al. (2012) analyzed lunar zircons by EBSD and found that microtwin formation occurred simultaneously with {112} PF development and was caused by a martensitic shear response to compression or extension.

The Vredefort Dome impact basin in South Africa is the oldest and largest precisely dated impact structure on Earth and is deeply eroded, exposing crustal granitoids and metamorphic rocks in the core of the central uplift of the complex crater (Gibson and Reimold 2008). Shocked zircon has been reported from a wide variety of bedrock lithologies at the Vredefort Dome (Kamo et al. 1996; Gibson et al. 1997; Moser 1997; Hart et al. 1999; Reimold et al. 2002; Flowers et al. 2003; Moser et al. 2011) and in sediments of the Vaal River and tributaries (Cavosie et al. 2010). The 2.02 Ga Vredefort impact age has been determined by U-Pb dating of recrystallized granular zircon, newly formed overgrowths on shocked grains, and also from newly crystallized zircons in impact melts (Kamo et al. 1996; Gibson et al. 1997; Moser 1997).

Methods

Sample collection and mineral separation

Thirty-two detrital shocked zircons from proximal and distal localities to the Vredefort Dome were analyzed in this study. Two colluvium samples were collected within the core of the structure; sample 09VD17 was collected along the base of a resistant low-lying ridge of granophyre dike intruding granitoid 0.5 km south of the town of Vredefort (S 27˚ 0.9', E 27˚ 22.681'). Sample 09VD21 was collected from the base of an Inlandsee Leucogranofels outcrop 1.5 km north of the Inlandsee Pan in the center of the dome (S 27˚ 2.870', E 27˚ 29.603'). Two alluvial samples were collected from the Vaal River; sample 07VD08 was collected within the Vredefort Dome, 25 km west of Parys (S 26˚ 58.250', E 27˚ 12.566' (see sample description in Cavosie et al. 2010). Sample 09VD42 was collected at a distal location in the Vaal River, 674 km downriver from the Vredefort Dome (S 28˚ 42.473', E 24˚ 4.478') near Schmidtsdrift. Samples of 1 to 2 kg of unconsolidated sediment were collected at each location. Heavy minerals were concentrated from the < 0.5 mm sediment fraction with heavy liquids. The heavy mineral fraction was then divided with a Frantz isodynamic magnetic separator to concentrate zircon.

Imaging external shock microstructures

Shock microstructures in thirty-two subhedral zircons, between 200 μm and 1000 μm in length, were identified with backscattered electron (BSE) imaging using a Cambridge Instruments Stereoscan 120 scanning electron microscope (SEM) in the Department of Physics at the University of Puerto Rico Mayagüez. Higher resolution BSE surface imaging was conducted in the Department of Geoscience at the University of Wisconsin-Madison, using a Hitachi S-3400 SEM with an accelerating voltage of 15 kV. Each grain was carefully placed along the c-axis, parallel to a {100} prism face, on 1-cm-diameter SEM stubs with carbon tape. After imaging the first external surface, grains were rotated 90˚ about the c-axis with tweezers and remounted to image the adjacent crystal face. This procedure was repeated until all four sides of the dominant tetragonal prism were imaged. Imaging all four prism faces provides a 360˚, three dimensional perspective of the grain, which facilitates modeling the orientation of PFs intersecting external crystal surfaces. The detrital zircons were not chemically treated to enhance the surface expression of the microstructure; all apparent etching is natural.

Imaging internal shock microstructures

After external imaging, the thirty-two grains were cast in a 2.54-cm epoxy grain mount in an orientation parallel to one of the four previously imaged prism faces. The mount was ground and polished using standard techniques, and given a final polish with 50 nm colloidal silica. Measurement of internal shock microstructures exposed in polished section was conducted at the Zircon and Accessory Phase Laboratory at Western University using a Hitachi SU6600 FEG-SEM. Low kV (5 kV) BSE images were collected using a five sector solid-state BSE detector, which reveals microstructural and chemical variations. Cathodoluminescence (CL) images were collected with a Gatan Chroma CL detector operating at 10 kV.

Electron backscatter diffraction (EBSD) maps (orthogonal grids of electron backscatter diffraction patterns) were collected with an Oxford Instruments Nordlys EBSD detector (Table 1) using the methodology of Moser et al. (2011). Three grains that contain a representative range of microstructures were selected for EBSD analysis (42-1-213, 17-158 & 17-197). Full grain EBSD maps with ~ 500 nm step size were made of each grain. Additional EBSD maps of smaller regions of interest were made using a ~100 nm step size (Table 1).

Crystallographic modeling of planar fracture orientations

Three dimensional digital zircon models were made using SketchUp 8, a freeware drafting program available from Google. Modeled zircon size and morphology (e.g. prisms and pyramid forms) were based on observed natural shocked grains. Different PF orientations, with rational crystallographic indices based on the unit cell spacing *a*=6.601 Å and *c*=5.98 Å (Robinson et al. 1971), were then added to the models. Modeled PF orientations include (010), (011), and all four {112}, including (112), $(1\bar{1}2)$, $(\bar{1}12)$ and $(\bar{1}\bar{1}2)$. Planar fractures were modeled with a consistent spacing of either 10 µm or 20 µm in an attempt to approximate the natural samples. Modeling the crystallographic orientations of PFs intersecting zircon crystal faces in three dimensions allows a direct comparison of the model with the planar microstructures in unknown orientations observed on the surfaces of naturally shocked zircons.

Results

Imaging the three dimensional relations of external PFs and correlating these to the internal microstructures of crystals mounted in known orientations resulted in the identification of seven orientations of PFs: (010), (100), (011), and four orientations of {112}. In addition, curviplanar fractures (CFs), matching those described as non-planar fractures (nPFs) by Cavosie et al. (2010) and CFs by Moser et al. (2011) were also identified on grain surfaces and correlated with internal microstructures. Modeling the intersection of various orientations of PFs with different zircon crystal forms (i.e. prisms and pyramids) confirmed the crystallographic orientations of all seven PF sets observed in the natural samples.

The following sections describe in detail the microstructure of three grains that represent the range of microstructures observed within the set of thirty-two detrital shocked zircons. Higher resolution images of the three featured grains are available in Appendix 1. External and internal images of the other twenty-nine zircons are listed in Appendix 2. A summary of all the observed microstructures is tabulated in Appendix 3.

Grain 42-1-213 (674 km downriver from Vredefort Dome)

External imaging and modeling results

Grain 42-1-213 is a ~380 µm long subhedral zircon that can be modeled as two equally sized interpenetrating {100} and {110} prisms, on which the intersection lineations produced by planar fractures in {112} can be illustrated (Fig. 1a). A total of six PF orientations are visible on the surface of the grain (Fig. 1). Three (hkl) orientations of planar fractures intersect the (100) face (Fig. 1b) and form linear features with negative relief, presumably due to preferential mechanical and/or chemical erosion of the defect-rich planes (Fig. 2a). Two of the (hkl) PF orientations appear to be conjugate with an acute angle of 49˚. The third (hkl) orientation of PFs are widely spaced and oriented at a higher angle to the c-axis relative to the conjugate set. The high angle PF set has accommodated a few microns of displacement resulting in visible offset of the crystal (Fig. 1b). The intersection lineations of the conjugate (hkl) fracture set with (100) can be traced onto the $(1\bar{1}0)$ face, where four sets of linear features are visible (Fig. 2). Two of the PF intersection lineations are conjugate with an acute angle of 65˚, whereas the third linear feature is at a right angle to the c-axis (Fig. 2a). A fourth set of linear features on $(1\bar{1}0)$ are conspicuous as the continuation of the widely spaced fractures visible on (100). Modeling the orientations of the closely spaced planar fractures in this grain demonstrates that all of the observed conjugate (hkl) orientations, including the differences in their angular relationships on different faces, can be explained by the interactions of four PF sets in {112} orientation (Figs. 1a, 2b). The four {112} PF orientations form two conjugate lineation sets that can be distinguished by acute angle; on all {100} faces the acute angle is 49˚; on all {110} faces the acute angle is 65˚ (Fig. 2). On {110} faces two of the {112} PFs are parallel and form lineations at a right angle to the c-axis. The orientation of the fifth (hkl) PF set was identified as (011) through modeling and observation of its intersections on all four sides of the grain (Figs. 1, 2). The sixth PF orientation, a c-axis parallel set, is identified as (h10) (Fig. 1d). The spacing of (h10) and {112} PFs is typically less than 5 µm, while the spacing of (011) PFs is > 30 µm. Furthermore, the (011) PFs offset the {112} PFs and therefore formed after the {112} PFs.

Internal microstructural analysis

A CL image of the polished section in (100) orientation shows typical igneous growth features, including oscillatory zoning with a convoluted dark core (Fig. 3). Crosscutting the CL pattern are light and dark PFs that correspond to externally visible $(\bar{1}12)$ and $(1\bar{1}2)$ PFs, and form an acute angle of 49˚ (Fig. 3e, PFs 1 & 3). Micron-scale offsets of the oscillatory zoning pattern along the {112} PFs show conjugate geometry with dextral offset of oscillatory zoning, indicating extensional deformation parallel to the c-axis of the grain (Fig. 3e). The (011) PFs show ~5 µm of offset of both the grain margin and oscillatory zoning, which indicates sinistral displacement if the slip vector was parallel to the plane of the section (Figs. 3a, b, PFs 4 & 5). In BSE {112} PFs appear as either discrete bright lines or dark cracks running through the grain (Fig. 3c). In EBSD {112} PFs have accommodated some misorientation and form low angle (1˚ to 5˚) grain boundaries (Fig. 3d). Some {112} PFs host, or are composed of, lamellae of zircon in twin orientation relative to the matrix; the twins are parallel, several hundred nanometers wide and extend over tens of microns. These microtwins are in the same orientation as the 65˚ (1k2) microtwins first described by Moser et al. (2011) (Figs. 3d, e) and the {112} microtwins reported by Timms et al. (2012) in lunar zircons. Here we show that microtwins occur as conjugate sets in $(\bar{1}12)$ and $(\bar{1}12)$ with the $(1\bar{1}2)$ microtwin having roughly twice the thickness (Fig. 3e). The narrow $(\bar{1}12)$ microtwins appear to have experienced dextral offset along the $(1\bar{1}2)$ plane (Fig. 3e). In contrast, PFs in (011) orientation form low angle boundaries that have accommodated up to ~10˚ of misorientation (Fig. 3d). While the c-axis parallel PFs are not visible in CL or BSE, narrow, linear domains of <1˚ misorientation were identified in (h10) orientation by EBSD (Fig. 3d).

Grain 17-158 (colluvium, center of the Vredefort Dome)

External imaging and modeling

Grain 17-158 is a 500 µm long subhedral crystal that can be modeled as a {100} prism truncated by {111} pyramids (Fig. 4a). The surface of the grain displays one set of deeply etched (010) PFs that can be seen on two parallel faces (Figs. 4b, d), but are not seen on the two perpendicular faces (Figs. 4c, e) indicating that only one {010} PF orientation is present. The orientation of the (010) PF set can be determined visually by observing the orientation of the intersection lineations of the PF with the {111} facets, as it remains parallel to the c-axis, ruling out all other (h10) orientations but (010). Two sets of conjugate high-angle (hkl) PFs are visible on all four {100} faces of the grain, forming an acute angle of 49˚, which is consistent with {112} PFs (Fig. 2b). This grain contains no {110} prism and it is therefore not possible to distinguish whether two or four conjugate {112} PFs are present [either (112) & $(\bar{1}\bar{1}2)$ or $(1\bar{1}2)$ & $(\bar{1}12)$]. The grain also contains a series of curviplanar fractures at a high angle to the c-axis (Fig. 4b).

Internal microstructural analysis

CL imaging of grain 17-158 shows a complex pre-impact zonation that is broadly concentric, with a conspicuous bright rim surrounding a dark core with irregular zoning (Fig. 5b). The dominant impact microstructures visible in CL are narrow bright bands crossing the grain that correspond to curviplanar fractures visible on the surface (Figs. 5a, b). Along the CL bright curviplanar fractures are localized CL dark areas that do not index as zircon in EBSD (Fig. 5f, CFs 2 & 3); this material is also seen in small patches branching along the planes of the (010) and {112} PF orientations. Small bands of CL bright material occur in one {112} orientation, but the conjugate {112} PF set is not visible in CL or BSE, even though a second {112} PF orientation is visible on the external surface (Figs. 5b, c). The BSE image (Fig. 5c) shows a dramatically different microstructure than the CL image. In BSE a prominent set of closely spaced (10 µm) (010) PFs is the dominant microstructure, and the conspicuous core-rim zoning observed in CL is not visible (Fig. 5, PF 1); the bright CL zones along the curviplanar fractures are also not evident in BSE. EBSD data confirm the presence of the prominent (010) PF orientation visible in surface (Fig. 5a) and BSE (Fig. 5c) imaging and show that this planar microstructure has accommodated low degrees (1-10˚) of rotation across the length of the grain (Fig. 5d). In the EBSD map, PFs along {112} occur in one orientation, and form low angle grain boundaries with >5˚ of misorientation (Fig. 5f) or microtwins (Figs. 5d, e, f). The microtwins in {112} orientation crosscut the (010) PFs and therefore postdate the development of (010) (Fig. 5f). The microtwins are ~200 nm in width and discontinuous (Figs. 5e, f). The curviplanar fractures are sub-parallel to the {112} PFs, and form low angle grain boundaries with up to 5˚ of misorientation that crosscut (010) grain boundaries (Fig. 5f). Both the (010) and {112} PFs have sub-µm widths, whereas the curviplanar fractures range up to 5 µm in width and contain recrystallized domains with discrete sub-grains up to 10 µm long that are oriented at high angles (~15˚) to the host zircon (Fig. 5f).

Grain 17-197 (colluvium, center of the Vredefort Dome)

External imaging and modeling

Grain 17-197 is 340 µm long and can be modeled as a {100} prism with complex interpenetrating pyramids that are rounded; the major pyramid form is {111}, but other faces are evident (Fig. 6). The grain exhibits one set of c-axis parallel PFs, which are visible on parallel {100} faces (Figs. 6b, d). The c-axis parallel PF set is in (010) orientation and displays >5 µm spacing. One high angle (hkl) PF set visible on all four prism faces can be modeled as {112} (Fig. 6). A second conjugate PF set, forming an acute angle of 49˚, is visible on (010) (Fig. 6c). The conjugate PF set does not appear on the other three prism faces, but does correspond to curviplanar fractures on those faces that are sub-parallel to {112} (Figs. 6b, d). The set of {112} PFs visible on all faces shows <5 µm spacing, whereas the second {112} PF/CF set has a broader spacing (~10 µm). The development of curviplanar fractures in this grain is thus associated with the conjugate {112} PF set.

Internal microstructural analysis

The interior of grain 17-197 exhibits igneous growth features, including oscillatory zoning (Fig. 7b). In CL the PFs in {112} orientation and curviplanar fractures can be seen crosscutting the grain and offsetting the igneous zonation (Fig. 7b, PFs 1, 2 & 3). The {112} PFs show a dark CL response, whereas the curviplanar fractures contain both dark and bright CL patches (Fig. 7b, CFs 4, 5 & 6). In BSE the {112} PFs are conspicuous bright linear features, while the curviplanar fractures form dark 'trails' crossing the grain (Fig. 7c). An incident UV light image shows that the curviplanar fractures exhibit a significantly different response than the host zircon, suggesting they are filled with other material (Fig. 7d, CF 6). The curviplanar fractures appear as dark red trails that completely cross the grain in three dimensions, whereas the two {112} PFs are not visible in UV (Fig. 7d). EBSD data reveal the presence of microtwins in {112} orientation (Figs. 7e, f, PFs 2 & 3) that correspond to the bright PFs visible in BSE (Fig. 7c). The microtwins are discontinuous and typically >500 nm in width. The {112} microtwins (PFs 2 & 3) are offset by up to one micron by the curviplanar fractures (Fig. 7f, CF 4), which form low angle grain boundaries with up to 4˚ of misorientation. Within the curviplanar boundaries are discrete zones of material that EBSD analysis was unable to index as zircon (Fig. 7f). Many of the curviplanar fractures are in {112} orientation, as they form acute angles of ~49˚ with the {112} PFs that contain microtwins (see Figs. 2; 7f, CF 4).

Discussion

The three-dimensional external surface imaging allows the determination of unique Miller indices for each set of planar microstructures through modeling. This approach has great value in that defect-rich PFs do not possess long range order and hence their crystallographic orientation cannot be reliably measured by diffraction techniques such as EBSD. Conversely, microstructural analysis of polished sections by EBSD allows measurement of crystallinity and strain at such boundaries at a resolution not otherwise achievable. Here we have taken advantage of the strengths of the two approaches to rigorously examine orientation and characteristics of PFs in shocked zircon eroded from the Vredefort Dome. Using internal and external documentation of microstructures, along with modeling, we now correlate multiple rational crystallographic PF orientations to specific styles of deformation, compare our results to published work, and interpret previously published shocked zircons in a crystallographic context. In addition, we suggest a revised nomenclature for planar microstructures in shocked zircon, and describe a chronologic framework for their development.

Correlating external and internal planar microstructures

Previous studies of planar microstructures in zircon have recognized the difficulty in correlating microstructures visible at the grain scale with microstructures visible at the sub-μm-scale in EBSD or TEM analyses (Leroux et al. 1999; Gucsik et al. 2002; Reimold et al. 2002; Moser et al. 2011; Timms et al. 2012). Cavosie et al. (2010) described PFs in five orientations in detrital shocked zircons from the Vredefort Dome, including (010), (100) and (001) and two un-indexed (hkl) sets. The three indexed PF orientations were determined visually from SEM images that show PFs intersecting multiple grain surfaces. Timms et al. (2012) identified planar microstructures in lunar zircons in five orientations, including {001}, two {110}, and two {112} forms. The modeling and detailed imaging results presented here increase the total number of unique PF orientations reported in naturally shocked zircon to ten, adding all four forms of {112} and (011).

(010) and (100) planar fractures

At least one set of c-axis parallel PFs is visible on the exterior of 84% of the grains (27 of 32) (e.g., (010)) and 34% of the grains (11 of 32) show a second (hk0) set perpendicular to the first (Fig. 8). Typically, c-axis parallel planar fractures show <10 μm spacing. EBSD analysis reveals that c-axis parallel PFs form low angle grain boundaries ranging from 1˚ to 10˚ of misorientation.

While c-axis parallel PFs are strikingly apparent on the exterior of some grains (e.g., Fig. 5), this microstructure is generally not visible in CL or BSE images of polished grains (e.g. grains 17-165, 17-183 & 21-245 in Appendix 2). Grain 17-158 shows well-developed (010) PFs internally, however between the two major curviplanar fractures (Fig. 5c, CFs #2, 3) the BSE response of (010) PFs is diminished. Additionally grain 21-245 (Appendix 2) preserves a small region of well-developed c-axis parallel PFs at one tip that are not found throughout the rest of the grain. Grains 17-165 and 17-183 (Appendix 2) also have well-developed external c-axis parallel PFs that are not visible internally. We speculate that the {010} microstructures annealed more readily than all other PF orientations, even though the crystal structure retains some physical manifestation of this microstructure as evidenced by the strong preferential etching of grain exteriors (Figs. 5b, e). In our model, (010) PFs in grain 17-158 represent an example of lesser annealed (010) PFs, whereas annealing in grains such as 17-165 completely erased the internal evidence of a c-axis parallel microstructure. Leroux et al. (1999) identified common {010} planar microstructures in zircon experimentally shocked to 20 GPa, and attributed the development of this microstructure to the glide system <100>{010} (Leroux et al. 1999). However, Timms et al. (2012) did not identify planar microstructures in (010) or (100) orientation in lunar zircon and speculated that this is due to low Young's modulus normal to {010} preventing development of PFs in this orientation. The well-developed {010} planar microstructures in the terrestrial shocked zircons described here suggest that intrinsic properties of zircon are not the main control on the formation of this microstructure.

In contrast to most studied grains, grain 17-158 exhibits an internally preserved c-axis parallel microstructure. The grain was collected at the base of a granophyre outcrop, a rock type that has been documented as part of the impact-derived melt injected downward into bedrock as evidenced by entrained surface xenoliths and xenocrysts from higher crustal levels (Therriault et al. 1996; Therriault et al. 1997). If grain 17-158 originated in granophyre, it is possible that the unusual c-axis parallel microstructure is preserved because this grain may have experienced a different shock regime and annealing history than other grains in the sediment sample. Alternatively, this microstructure may have developed due to the orientation of the c-axis with respect to the shockwave. In the experimental study of Leroux et al. (1999), {010) PFs developed with the shock wave propagating parallel to the c-axis; how planar microstructures change due to varying the angle of the incoming shock wave with respect to the c-axis is not known, and beyond the scope of this study. The physical properties and interactions with neighboring mineral phases are other considerations, but cannot be evaluated for detrital shocked zircons that lack petrographic context.

{112} planar fractures

The most common planar microstructures visible on grain exteriors are {112} PFs (Fig. 8). Up to four orientations (the maximum possible) of {112} PFs were documented in one grain, including (112), $(1\bar{1}2)$, $(\bar{1}12)$ and $(\bar{1}\bar{1}2)$ (Fig. 2). All of the grains in this study exhibit at least one set of {112} PFs, and 94% (30 of 32) display two {112} PF sets. However, the population of zircons is dominated by {100} prisms, and it is therefore not possible to discern whether two or four sets of {112} are present for the majority (31 of 32) of grains. This is because (112) and $(1\bar{1}2)$ PF sets are parallel to one another when viewed on (100); likewise, the $(\bar{1}\bar{1}2)$ and $(\bar{1}12)$ PF sets are also parallel when viewed on (100) (Fig. 2b). The parallelism of the four {112} PF orientations causes a maximum of only two {112} PFs to be visible on any {100} prism face, even when four are present (Fig. 2b). Only zircons expressing both {010} and {110} prisms allow the identification of all four {112} PF orientations through observation of the interactions of PFs on adjacent faces (Fig. 2). The surface expression of PF spacing is variable across a grain (e.g. Fig. 1) as noted in observation of natural samples and in models of {112} PFs. This apparent non-uniform spacing can be attributed to the interaction of (apparent) parallel PFs on various faces of the grains [e.g. (112) and $(1\bar{1}2)$ on (100) faces], causing variable spacing (compare the natural sample and crystal model in Fig. 2). Because of this parallelism of different {112} lineations on {100} faces, determining the “true” spacing of {112} PFs cannot be done reliably from either surface imaging or analysis of a polished section but may be possible through modeling. We also note that {112} PFs are readily identified in previously published external images of shocked zircons. Kamo et al. (1996; their Fig. 4a) reported a shocked grain from Vredefort bedrock that displays two PF sets crosscutting at an acute angle of 49˚, typical of {112} sets on a {100} form. Detrital shocked zircons with PFs at the

(DOI will not work until issue is live.) DOI: http://dx.doi.org/10.2138/am.2013.4165

Vredefort Dome also display conjugate {112} PFs crosscutting a {100} form (Cavosie et al. 2010, their Figs. 5e, f). At Sudbury Krogh et al. (1996, their plate 1b) reported shocked zircon from the Levack gneiss that also displays {112} PFs in at least two orientations.

Internally, {112} PFs are the most common visible shock microstructure; 78% (25 of 32) of the grains display one {112} set, and 41% (13 of 32) display a conjugate {112} PF set (Fig. 8). In this study all internal images are of polished sections parallel to {100} prism faces. As a consequence, a maximum number of two {112} PF orientations are visible, even in grains with four {112} PF sets present on the grain surface. In contrast, grains polished parallel to {110} can show up to three {112} PF orientations internally. Therefore, by mounting zircons along {100} faces, as is common, one will underestimate the number of {112} PFs.

EBSD analysis reveals that PFs in {112} orientation form low-angle grain boundaries with 1˚ to 10˚ of misorientation. Microtwin lamellae were observed in two different {112} orientations, and one set could be identified offsetting the other with up to 100 nm of apparent displacement (Figs. 3d, e). Microtwins range in width from 100 nm to 500 nm and are generally discontinuous across the grains. Microtwin development thus was either incomplete during initial formation, or alternatively post-shock temperatures at the Vredefort Dome partially annealed the microtwins. It is possible that {112} PFs first develop as low-angle grain boundaries but as motion continues along these planes the shear stress is accommodated through 65˚ rotation about <110> (Moser et al. 2011). Timms et al. (2012) noted that {112} PFs are normal to directions of high Young's modulus and that the microtwins are likely formed by martensitic shear causing short-range shortening of the crystal lattice.

(011) planar fractures

Unlike other PF orientations, (011) PFs form widely spaced (30 μm) fractures on grain surfaces, and crosscut both {112} and c-axis parallel PFs. Internally, (011) PFs form well developed low angle grain boundaries showing as much as 10˚ of misorientation. The most significant feature of (011) PFs are the large offsets of the CL zoning (Fig. 3b); as much as 5 μm of apparent offset can be identified along (011) PFs. The (011) PFs were only observed in 6% of the grains (2 of 32) (Fig. 8).

Curviplanar fractures

Curviplanar fractures show a variety of orientations, but typically are found in orientations sub-parallel to {112} (e.g., Fig. 7f). Internally, curviplanar fractures disturb CL zonation forming both anomalously dark and bright patches. In BSE images, curviplanar fractures form 'trails' of relatively low atomic number ovoid forms (e.g. Fig. 5c). These forms can be found branching from the curviplanar fractures to both {112} and (010) PFs (Figs. 5f, 7f). It has previously been suggested that curviplanar fractures may serve as injection pathways for melt during crater formation (c.f., Moser et al 2011). Moser et al. (2011) identified inclusion trails of alkali Si-Al glass along the curviplanar fractures and interpreted these as injected, shock induced partial melt of the host granitoid gneiss. In grain 17-197 inclusion trails crosscut the entire grain, and can be observed below the polished surface with UV imaging (Fig. 7d). Gibson et al. (1997, their Fig. 5) reported an inherited shocked core with PFs and curviplanar fractures surrounded by an unshocked rim from the Central Granite at the Vredefort Dome.

Endogenic origin of planar microstructures in zircon?

Austrheim and Corfu (2009) identified apparent 'planar deformation features' in zircon from a non-impact generated fault zone in SW Norway. The authors interpret a series of sub-parallel fractures and anomalous sieve texture to be analogous to impact produced PFs in zircon. While the planar microstructures are superficially similar to planar microstructures described here, additional aspects, including crystallographic orientation, presence of low-angle grain boundaries, and microtwins should be documented before these microstructures can be considered endogenic equivalents of the high pressure planar microstructures observed in shocked zircons from impact environments.

Zircon twinning and reidite

Zircon twins

The microtwins documented in this study occur as multiple alternating contact twins along parallel {112} compositional planes, and thus fit the precise definition for polysynthetic twins. To our knowledge, this is the first report of polysynthetic twinning in zircon, which appears to be a unique hallmark of impact processes. The microtwins along two different orientations of {112} identified in this study are the same 65˚ microtwin on {1k2} first reported by Moser et al. (2011) and in {112} by Timms et al. (2012). Timms et al. (2012) noted that while the 65˚ rotation of the zircon lattice about <110> translates <112> about {110}, the twin mechanism is likely considerably less than 65˚ of actual rotation as this microstructure is accommodated by short-range lattice reconfiguration caused by martensitic shear. Leroux et al. (1999) reported shock produced twins, however they occurred within the high pressure polymorph reidite, not within the host zircon. The absence of twin formation in zircon in the experiments of Leroux et al. (1999) is difficult to reconcile with their (seemingly) ubiquitous presence in shocked zircons at the Vredefort Dome.

Reidite

Reidite was not identified during EBSD mapping of the three grains in this study, and has not previously been reported in shocked zircons from the Vredefort Dome analyzed by EBSD (Moser et al., 2011) and TEM (Reimold et al., 2002). Leroux et al. (1999) identified reidite in zircon experimentally shocked at 40 GPa and above. This suggests that either shock pressures affecting the zircons in this study were below the ca. <40 GPa zircon-reidite transformation (Leroux et al. 1999) or, if originally present, post-impact temperatures were high enough to convert the impact-formed reidite back to zircon. Kusaba et al. (1985) found that above 1200˚ C reidite converted back to zircon. Temperatures in excess of 1200˚C were likely attained near the center of the Vredefort Dome (Gibson, 2002), although the extent of exposed bedrock that experienced these high temperatures is not known. Zircons from bedrocks in this central region were recently characterized as ‘hot-shock” zircons by Moser et al. (2011), based on demonstrated Pb-loss.

The observation that original igneous zoning is preserved in many shocked zircons suggests that these grains did not experience conversion to reidite and subsequent reversion back to zircon, although the effect of these phase transitions on trace element distribution in zircon has not been described previously. There is no *a priori* reason to associate the presence of {112} twins in zircon and the possible former presence of reidite, such as a conversion of the host zircon to reidite followed by a subsequent reversion back to zircon that is twinned in the process. The {112} orientation of the zircon microtwins, as described above, is inconsistent with the planes along which reidite developed in the experimentally shocked zircons of Leroux et al. (1999). The reidite documented by Leroux et al. (1999) formed along {100} planes in zircon, not {112}. More critically, the twins documented by Leroux et al. (1999) were found within the (112) orientation of reidite; no twins were found within the host zircon. Several high pressure experiments have shown that the zircon-reidite transition occurs near 20 GPa (e.g., Knittle and Williams, 1993). However other experiments have shown that the presence of impurities (van Westernen et al. 2004) and radiation damage (Lang et al. 2008) expand the stability of zircon to significantly higher pressures; van Westernen et al. (2004) found no reidite in their irradiated zircons at 37 GPa. Thus applicability of experimentally derived phase relations for zircon-reidite to natural, impurity and radiation damaged zircon remains unclear. Given the differences among experimental results, and also between experimental results and measurements of natural samples, it is difficult to determine if reidite was originally present in the grains from this study; no evidence was found to support the interpretation that it was ever present in these grains.

Proposed planar microstructure nomenclature for zircon

The nomenclature used to describe planar microstructures in zircon is highly variable in published studies, and includes terms such as ‘planar features’ (Krogh et al. 1984), ‘planar deformation features (PDFs)’ (Bohor et al. 1993), ‘planar microstructures’ (Kamo et al. 1996) and ’planar fractures’ (Cavosie et al. 2010). This diversity of terms is understandable, and is reminiscent of the historical development of documenting shock microstructures in quartz (Alexopolous et al. 1988; Stöffler and Langenhorst 1994). The current situation with zircon is largely due to inconsistent application of nomenclature developed for shocked quartz being used to describe shocked zircon. In the SiO_2 system, PDFs *sensu stricto* are explicitly defined by TEM observation as either (1) shock produced lamellae of amorphous silica or (2) basal Brazil twins (Stöffler and Langenhorst 1994, their Table 4). In contrast planar fractures (PFs) in quartz are defined as sets of parallel open or closed fissures in specific crystallographic orientations with a larger spacing than PDFs (Stöffler and Langenhorst 1994).

The characteristics of planar fracture (PF) in zircon described here closely match those for PFs in quartz in that they are open or filled planar microstructures that occur in specific crystallographic orientations and do not contain amorphous $ZrSiO_4$. We propose adoption of the general term 'planar fracture' for all planar microstructures identified on the surface of or within shocked zircons. We suggest that the term 'planar deformation feature' be used only when amorphous $ZrSiO_4$ lamellae are documented, as is the case with shocked quartz, however we note that amorphous lamellae have not yet been identified in naturally shocked zircon. Timms et al. (2012) used the term 'PDF' for all planar microstructures in (001), {110}, {112}, although they do not demonstrate the presence of amorphous $ZrSiO_4$ lamellae. The authors identify weakened EBSD band contrast signals in orientations of planar microstructures; however it is not possible to determine whether this is caused by an elevated concentration of lattice defects or thoroughly amorphous $ZrSiO_4$ at this scale of observation. A better description of the nature and crystallographic orientation of 'true' PDFs in zircon (i.e. amorphous lamellae of $ZrSiO_4$) awaits their discovery in natural samples (cf. Leroux et al. 1999). The term 'microtwin' was introduced by Moser et al. (2011) and this microstructure has since been found by Timms et al. (2012) and this study. Microtwins can be documented by EBSD and TEM, appear to only occur within {112} orientations, and form simultaneously with {112} PF development.

Chronology of microstructure formation during impact basin evolution

The results of this microstructural investigation build on the results of Moser et al. (2011) and allow the diversity of different shock microstructures of zircon that form during the evolution of an impact basin to be placed in a chronological sequence based on crosscutting relations. The earliest microstructure that formed in our sample set are c-axis parallel planar fractures, including (010) and (100), as all other microstructures appear to crosscut the c-axis parallel PFs. The c-axis parallel PFs also show the poorest preservation in polished section, suggesting that they may be rapidly annealed. The next microstructures to form are {112} PFs, which are preserved as low-angle grain boundaries. The {112} PFs form after the c-axis parallel PFs since the {112} microtwins crosscut the c-axis parallel PFs (Fig. 5f). The {112} PFs contain up to two orientations of microtwins; consistent extensional offset relations observed in different grains suggest that the two {112} twin orientations do not form simultaneously. Moser et al. (2011) proposed that microtwin formation occurs during rarefaction of the shockwave (Melosh 1989). The {112} microtwins and low-angle grain boundaries are crosscut and offset by (011) PFs and curviplanar fractures.

Curviplanar fractures were found to predate {1k2} PFs by Moser et al. (2011). In contrast, we observe curviplanar fractures that postdate and offset the {112} PFs by as much as 1 µm (Fig. 7f, CF 4) and also crosscut {010} microstructures (Fig. 5f, CF 3). It is unclear yet whether the chronology of CF formation is due to reactivation of early fractures or whether there were mulitiple stages of curviplanar fracture formation during shock loading and unloading. Moser et al. (2011) identified melt inclusions along curviplanar fractures and we find evidence of a similar relationship, whereby suspected melt remnants occupy curviplanar fractures (Fig. 7d, Appendix 1.4c), which suggests that melt injection is co-genetic with curviplanar fracture development. The included material (suspected to be melt) can also be seen branching from curviplanar fractures into c-axis parallel fractures in grain 17-185 and into {112} PFs in grain 17-197, signifying that other PFs were still open (i.e. not annealed) during melt injection, which indicates that the (010), (100), {112}, curviplanar fractures and melt microstructures formed over a short interval. The injection of melt along the PFs may be responsible for the incomplete nature of the microtwins, and in conjunction with external heat, contribute to the annealing of the earlier formed microstructures, particularly (010). The evolution of curviplanar fractures and injected melts is currently the subject of more detailed investigation.

The last planar microstructure to form is along (011). On grain surfaces (011) PFs are conspicuous, and can be seen crosscutting and offsetting {112} PFs (Fig. 1e). Melt inclusions were not observed on (011), suggesting that (011) PF formation post-dated melt injection (Fig. 3).

Concluding Remarks

Observation and correlation of the three dimensional relationships of external and internal planar microstructures are necessary to fully describe the dynamic shock deformation recorded in zircon. One caveat that results from this study is the recognition that in many cases, the total number of PFs documented will likely be underestimated using standard imaging techniques. When imaging grain surfaces, only zircons that express both {100} and {110} prism faces will allow the determination of the actual number of {112} PFs present due to parallelism of the {112} PF lineations on common crystal faces. In polished section, the actual number of PF orientations cannot be determined in any zircon by any method, due also to the parallelism of the {112} PFs described above.

The results of this study show that regardless of orientation, planar microstructures visible at the grain scale in shocked zircons are dominantly fractures; amorphous $ZrSiO_4$ lamellae were not identified. We favor the term 'planar fracture' for these microstructures, as continued reference to these features as 'PDFs' will likely result in confusion given the well-established application of this term for amorphous lamellae of SiO_2 in shocked quartz.

Acknowledgements

TME would like to thank the Barringer Family and the Planetary Division of GSA for receiving the Barringer and the Eugene M. Shoemaker awards. AJC acknowledges support from the National Science

Foundation (EAR-0838300). John Valley, Clark Johnson, John Fournelle, and Dayanidi Ortiz are thanked for providing access to sample processing facilities and laboratories at the Wisconsin Astrobiology Research Consortium (WARC) at the University of Wisconsin. Final thanks to Raiza Quintero and Lisa Cupelli for their support. We thank Anton Chakhmouradian for the editorial handling of this paper, and Axel Wittmann and an anonymous reviewer for their comprehensive and thorough reviews that helped to enhance the manuscript.

References cited

Alexopoulos, J.S., Grieve, R.A.F. and Robertson, P.B. (1988) Microscopic lamellar deformation features in quartz: Discriminative characteristics of shock-generated varieties. Geology, 16, 796-799.

Austrheim, H., and Corfu, F. (2009) Formation of planar deformation features (PDFs) in zircon during coseismic faulting and an evaluation of potential effects on U-Pb systematics. Chemical Geology, 261, 25-31.

Cavosie, A.J., Quintero, R.R., Radovan, H.A., and Moser, D.E. (2010) A record of ancient cataclysm in modern sand: shock microstructures in detrital minerals from the Vaal River, Vredefort Dome, South Africa. Geological Society of America Bulletin, 112, 1968-1980.

El Goresy, A., (1965) Baddelyite and its significance in impact glasses. Journal of Geophysical Research, 70, 3453-3456.

Erickson, T.M., Cavosie, A.J., Radovan, H.A., Moser, D.E., and Wooden J. (2011) Microstructural and isotopic constraints on impact basin provenance of detrital shocked minerals in the Vaal River, South Africa. 42nd Lunar and Planetary Science Conference, 2208.

Flowers, R.M., Moser, D.E., and Hart, R.J. (2003) Evolution of the amphibolite-granulite facies transition exposed by the Vredefort impact structure, Kaapvaal craton. South African Journal of Geology, 92, 223-234.

French, B.M. (1998) Traces of Catastrophe: A Handbook of Shock-Metamorphic Effects in Terrestrial Meteorite Impact Structures. Houston, TX, Lunar and Planetary Institute, 120p.

French, B.M. and Koeberl, C. (2010) The convincing identification of terrestrial meteorite impact structures: What works, what doesn't and why. Earth-Science Reviews, 98, 123-170.

Gibson, R.L. (2002) Impact-induced melting of Archean granulites in the Vredefort Dome, South Africa. 1: anatexis of metapelitic granulites. Journal of Metamorphic Geology, 20, 57-70.

This is a preprint, the final version is subject to change, of the American Mineralogist (MSA)
Cite as Authors (Year) Title. American Mineralogist, in press.
(DOI will not work until issue is live.) DOI: http://dx.doi.org/10.2138/am.2013.4165

Gibson, R.L., Armstrong, R.A., and Reimold, W.U. (1997) The age and thermal evolution of the Vredefort impact structure: A single-grain U-Pb zircon study. Geochimica et Cosmochimica Acta, 61, 1531-1540.

Gibson R.L., and Reimold, W.U. (2008) Geology of the Vredefort Impact Structure; A Guide to Sites of Interest, Council of Geoscience, Pretoria, South Africa, Memoir 97, 181p.

Glass, B.P. and Liu, S. (2001) Discovery of high-pressure $ZrSiO_4$ polymorph in naturally occurring shock-metamorphosed zircons. Geology, 29, 371-372.

Glass, B.P., Liu, S., and Leavens P.B. (2002) Reidite: an impact-produced polymorph of zircon found in marine sediments. American Mineralogist, 87, 562-565.

Gucsik, A., Koeberl, C., Brandstatter, F., Reimold, W.U., and Libowitzky, E. (2002) Cathodoluminescence, electron microscopy, and Raman spectroscopy of experimentally shock-metamorphosed zircon. Earth and Planetary Science Letters, 202, 495-509.

Hart, R.J., Moser, D., and Andreoli, M.A.G. (1999) Archean age for the granulite metamorphism near the center of the Vredefort Structure, South Africa. Geology, 7, 1091-1094.

Kamo, S.L., Reimold, W.U., Krogh, T.E., and Colliston, W.P. (1996) A 2.023 Ga age for the Vredefort impact event and a first report of shock metamorphosed zircons in pseudotachylitic breccias and granophyre. Earth and Planetary Science Letters, 144, 369-388.

Knittle, E. and Williams, Q. (1993) High-pressure Raman spectroscopy of $ZrSiO_4$: Observations of the zircon to scheelite transition at 300 K. American Mineralogist, 78, 245-252.

Krogh T.E., Davis, D.W., and Corfu, F. (1984) Precise U-Pb zircon and baddelyite ages for the Sudbury area. In E.G. Pye, A.J. Naldrett, and P.E. Giblin, Eds., The Geology and Ore Deposits of Sudbury Structure, 1, 431-447. Ontario Geological Survey, London, Ontario.

Krogh T.E., Kamo, S.L., and Bohor, B.F. (1993) Fingerprinting the K/T impact site and determining the time of impact by U-Pb dating of single shocked zircons from distal ejecta. Earth and Planetary Science Letters, 119, 425-429.

Krogh, T.E., Kamo, S.L., and Bohor, B.F. (1996) Shock metamorphosed zircons with correlated U-Pb discordance and melt rocks with concordant protolith ages indicate an impact origin for the Sudbury structure. In A. Basu and S. Hart, Eds., Earth Processes: Reading the Isotopic Code, 95, 343-353. American Geophysical Union, Washington, D.C.

Kusaba, K., Syono, Y., Kikuchi, M., and Fukuoka, K. (1985) Shock behavior of zircon: phase transition to scheelite structure and decomposition. Earth and Planetary Science Letters, 72, 433-439.

Lang, M., Zhang, F., Lian, J., Trautmann, C., Neumann, R., and Ewing R.C. (2008) Irradiation-induced stabilization of zircon ($ZrSiO_4$) at high pressure. Earth and Planetary Science Letters, 269, 291-295.

Leroux, H., Reimold, W.U., Koeberl, C., Hornemann, U., and Doukhan, J.-C. (1999) Experimental shock deformation in zircon: a transmission electron microscopic study. Earth and Planetary Science Letters, 169, 291-301.

Melosh, H.J. (1989) Impact Cratering: A geologic Process. Oxford Monographs on Geology and Geophysics, 11, 245p.

Moser, D.E. (1997) Dating the shock wave and thermal imprint of the giant Vredefort impact, South Africa. Geology, 25, 7-10.

Moser, D.E., Cupelli, C.L., Barker, I.R., Flowers, R.M., Bowman, J.R., Wooden, J., and Hart, J.R. (2011) New zircon shock phenomena and their use for dating and reconstruction of large impact structures revealed by electron nanobeam (EBSD, CL, EDS) and isotopic U-Pb and (U-Th)/He analysis of the Vredefort Dome. Canadian Journal of Earth Science, 48, 117-139.

Moser, D.E., Davis, W.J., Reddy, S.M., Flemming, R.L., and Hart, R.J. (2009) Zircon U-Pb strain chronometry reveals deep impact-triggered flow. Earth and Planetary Science Letters, 227, 73-79.

Nemchin, A., Timms, N., Pidgeon, R., Geisler, T., Reddy, S., and Meyer, C. (2009) Timing of crystallization of the lunar magma ocean constrained by the oldest zircon. Nature Geoscience, 2, 133-136.

Pidgeon, R.T., Nemchin, A.A., and Kamo, S.L. (2011) Comparison of structures in zircons from lunar and terrestrial impactites. Canadian Journal of Earth Science, 48, 107-116.

Reddy, S.M., Timms, N.E., Pantleon, W., and Trimby, P. (2007) Quantitative characterization of plastic deformation of zircon and geological implications. Contributions to Mineralogy and Petrology, 153, 625-645.

Reid, A.F. and Ringwood, A.E. (1969) Newly observed high pressure transformations in Mn_3O_4, $CaAl_2O_4$, and $ZrSiO_4$. Earth and Planetary Science Letters, 6, 205-208.

Reimold, W.U., Leroux, H., and Gibson, R.L. (2002) Shocked and thermally metamorphosed zircon from the Vredefort impact structure, South Africa: a transmission electron microscopic study. European Journal of Mineralogy, 14, 859-868.

Robinson, K., Gibbs, G.V., and Ribbe, P.H. (1971) The structure of zircon: a comparison with garnet. American Mineralogist, 56, 782-790.

Stöffler, D. and Langenhorst, F. (1994) Shock metamorphism of quartz in nature and experiment: I. Basic observation and theory, Meteoritics and Planetary Science, 29, 155-181.

Therriault, A.M., Reimold, W.U., and Reid, A.M. (1996) Field relations and petrography of the Vredefort Granophyre. South African Journal of Science, 99, 1-21.

Therriault, A.M., Reimold, W.U., and Reid, A.M. (1997) Geochemistry and impact origin of the Vredefort Granophyre. South African Journal of Science, 100, 115-122.

Timms, N.E., Reddy, S.M., Healy, D., Nemchin, A.A., Grange, M.L., Pidgeon, R.T., and Hart, R. (2012) Resolution of impact-related microstructures in lunar zircon: A shock-deformation mechanism map. Meteoritics and Planetary Science, 47, 120-141.

Van Westrenen, W., Frank, M.R., Hanchar, J.M., Fei, Y., Finch, R.J., and Zha, C-S. (2004) In situ determination of the compressibility of synthetic pure zircon (ZrSi04) and the onset of the zircon-reidite phase transition. American Mineralogist, 89, 197-203.

Wittmann, A., Kenkmann, T., Schmitt, R.T., and Stöffler, D. (2006) Shock-metamorphosed zircon in terrestrial impact craters. Meteoritics and Planetary Science, 41, 433-454.

Figure Captions

Figure 1. External images of detrital shocked grain 42-1-213 from the Vaal River, South Africa, 674 km downriver from the Vredefort Dome. (a) Model of zircon grain with interpenetrating {100} and {110} prisms and {101} pyramids, displaying four sets of {112} microstructures at 20 μm spacing and two (011) PFs at 30 μm spacing. (b-e) Exterior BSE images of grain 42-1-213 with labeled PF orientations. Straight arrows indicate PF orientations. See enlarged images in Appendix 1.

Figure 2. Comparison of grain 42-1-213 planar microstructures with modeled {112} and (011) PFs. (a) Exterior BSE image showing four orientations of {112} and the different angular relations of the conjugate {112} PFs on (100) (49˚) and $(1\bar{1}0)$ (65˚). (b) Model showing the angular relations and intersections of four {112} orientations on (100) and $(1\bar{1}0)$. Note that {112} PFs were modeled with 20 μm spacing, but (112) and $(\bar{1}\bar{1}2)$ are offset from $(1\bar{1}2)$ and $(\bar{1}12)$ by 10 μm.

Figure 3. Internal images of grain 42-1-213. (a) Exterior image of the face exposed in the polished section. White outline shows the location of the polished section. (b) CL image showing oscillatory zoning that is offset in different orientations along planar fractures. (c) BSE image showing {112} and (011) PFs. (d) A combined band contrast, local misorientation and grain boundary EBSD map. (e) Close up EBSD map showing 2 crosscutting sets of microtwins along {112}, 65˚ grain boundaries are colored red, the grey material within the grain boundaries is in the twinned orientation.

Figure 4. External images of detrital shocked grain 17-158 from the center of the Vredefort Dome. (a) Model of a zircon {100} prism with {111} pyramids. The model features four orientations of {112} PFs and one (010) PF set, all with 10 μm spacing. (b-e) Exterior BSE images of grain 17-158. Straight arrows indicate PF orientations, and curved arrows indicate curviplanar fractures (CF). See enlarged images in Appendix 1.

Figure 5. Internal images of grain 17-158. (a) Exterior image of the face exposed in polished section. The white outline shows the location of the polished section. (b) CL image showing core-rim zoning and various shock microstructures. Note the lack of c-axis parallel microstructures. (c) BSE image showing well developed (010) PFs. The round white splotches are an artifact of an uneven carbon coat. (d) A combined band contrast, local misorientation and grain boundary EBSD map. (e) Close up EBSD map showing microtwins in {112} orientation, (010) PFs and curviplanar fractures. (f) Close up EBSD map showing microtwins, c-axis parallel PFs and curviplanar fractures, 65˚ grain boundaries are colored red, the grey material within the grain boundaries is in the twinned orientation.

Figure 6. External images of detrital shocked zircon grain 17-197 from the center of the Vredefort Dome. (a) Model of a zircon {100} prism with {111} pyramid. The model features four orientations of {112} PFs at 10 μm spacing. (b-e) Exterior BSE images of grain 17-197. Straight arrows indicate PF orientations, curved arrows indicate curviplanar fractures. See enlarged images in Appendix 1.

Figure 7. Internal images of grain 17-197. (a) Exterior image of the face exposed in the polished section. The white outline shows the location of the polished section. (b) CL image showing oscillatory zoning that is offset in a dextral sense by {112} PFs. Curviplanar fractures in an approximately conjugate (49˚) orientation to {112} are also visible. (c) BSE image showing one orientation of {112} PFs and one orientation of curviplanar fractures in approximately conjugate {112} orientation. (d) Incident UV light image. The host zircon is largely translucent and PFs in {112} are not visible. Curviplanar fractures in

This is a preprint, the final version is subject to change, of the American Mineralogist (MSA)
Cite as Authors (Year) Title. American Mineralogist, in press.
(DOI will not work until issue is live.) DOI: http://dx.doi.org/10.2138/am.2013.4165

sub-{112} orientation show distinctly dark zones, indicating they are filled with material that is not zircon. (e) A combined band contrast, local misorientation and grain boundary EBSD map. (f) EBSD close up map showing {112} microtwins offset by curviplanar fractures, 65˚ grain boundaries are colored red, the grey material within the grain boundaries is in the twinned orientation.

Figure 8. Histogram of PF orientations for the 32 detrital shocked zircons imaged in this study. (a) Exterior PF orientations. (b) Interior PF orientations. Note that grains were mounted parallel to {100} prisms and therefore it is not possible to determine a second c-axis parallel PFs orientation (e.g., (100)) or uniquely differentiate the 3rd and 4th {112} sets.

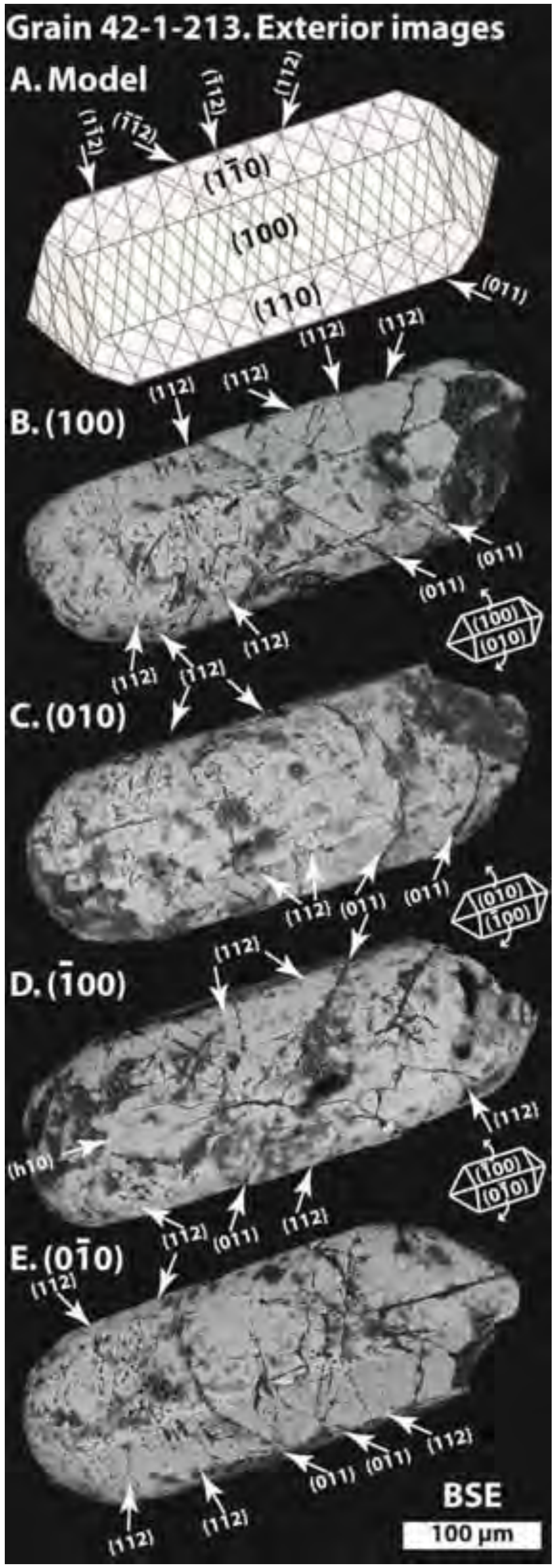
Grain 42-1-213. Exterior images
A. Model
(100)
(110)
B. (100)
C. (010)
BSE
100 μm

Figure 1

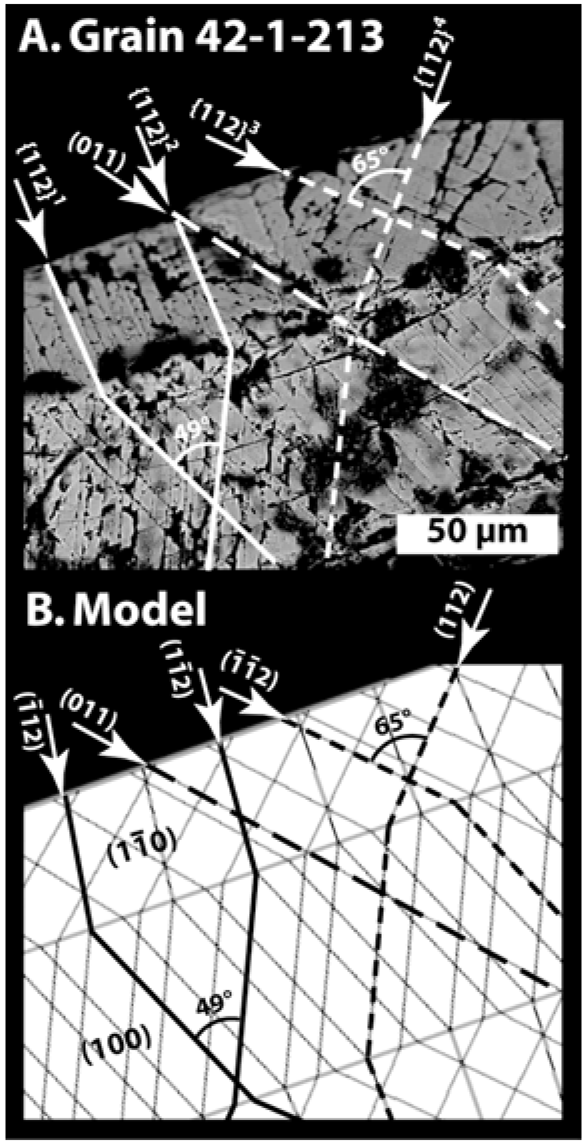
A. Grain 42-1-213
{112}¹
(011)
{112}²
{112}³
{112}⁴
65°
49°
50 μm
B. Model
(1̄12)
(011)
(11̄2)
(1̄1̄2)
(112)
65°
(11̄0)
49°
(100)

Figure 2

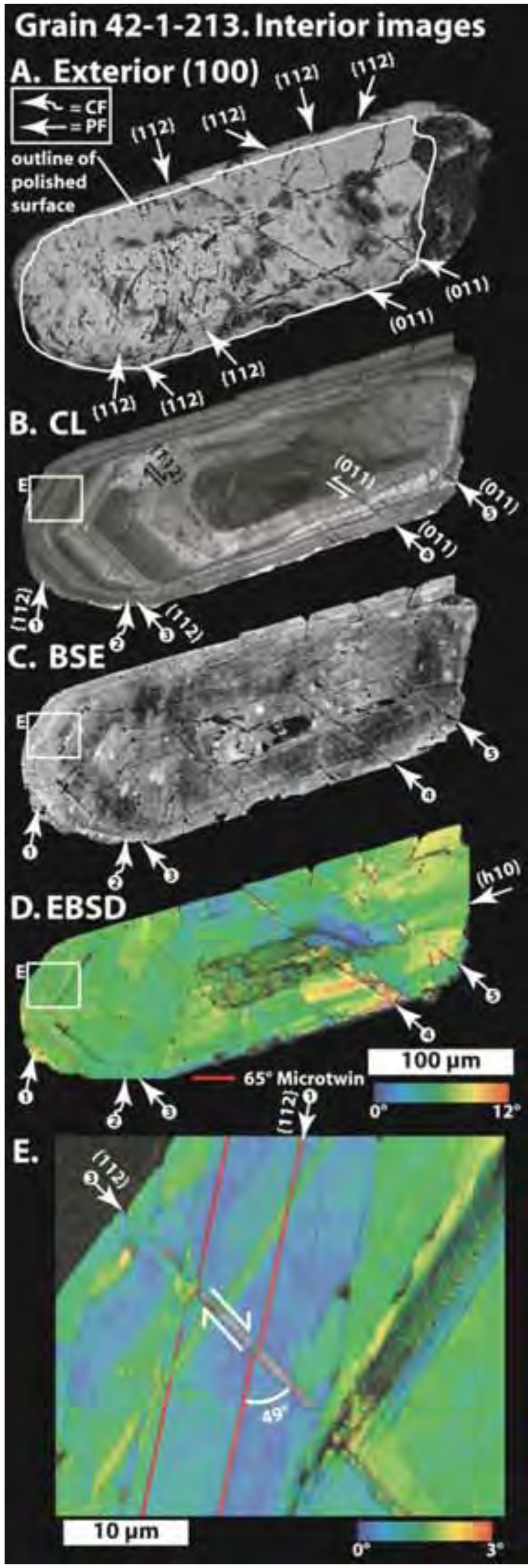
Grain 42-1-213. Interior images
A. Exterior (100)
= CF
= PF
outline of polished surface
{112}
{011}
B. CL
C. BSE
D. EBSD
(h10)
65° Microtwin
100 µm
0°
12°
E.
49°
10 µm
3°

Figure 3

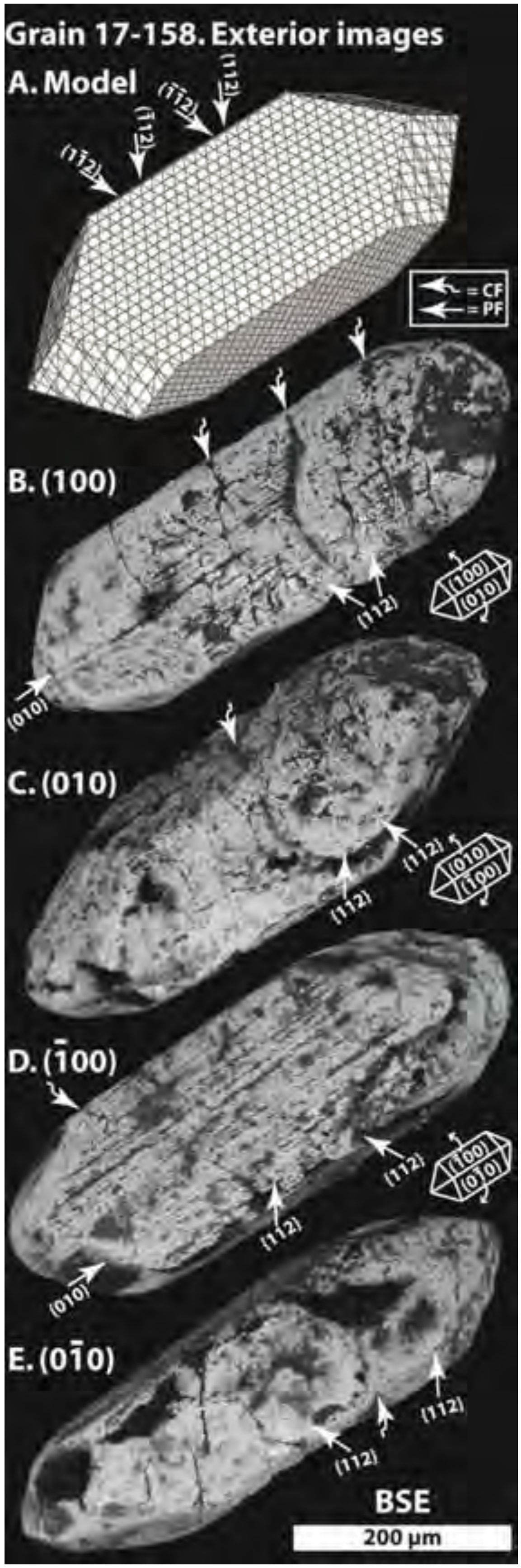
Grain 17-158. Exterior images
A. Model
B. (100)
C. (010)
D. (1̄00)
E. (01̄0)
= CF
= PF
BSE
200 μm

Figure 4

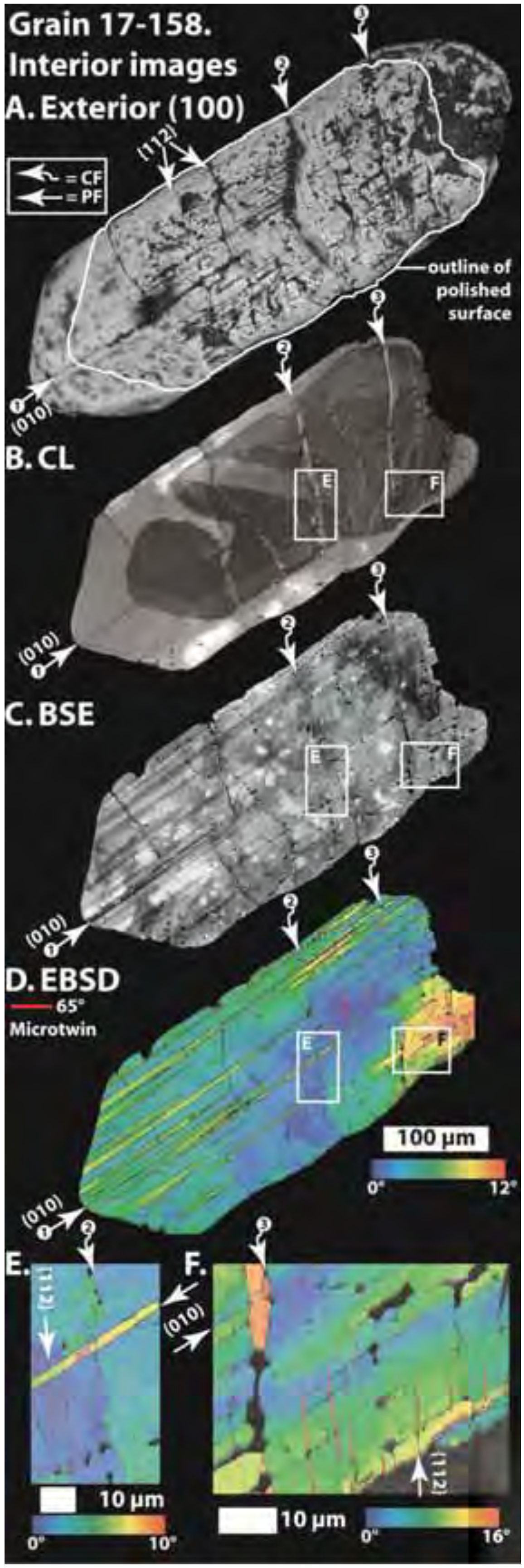
Grain 17-158.
Interior images
A. Exterior (100)
= CF
= PF
(112)
outline of polished surface
(010)
B. CL
E
F
C. BSE
D. EBSD
65°
Microtwin
100 µm
0°
12°
E.
F.
(112)
(010)
10 µm
0°
10°
16°

Figure 5

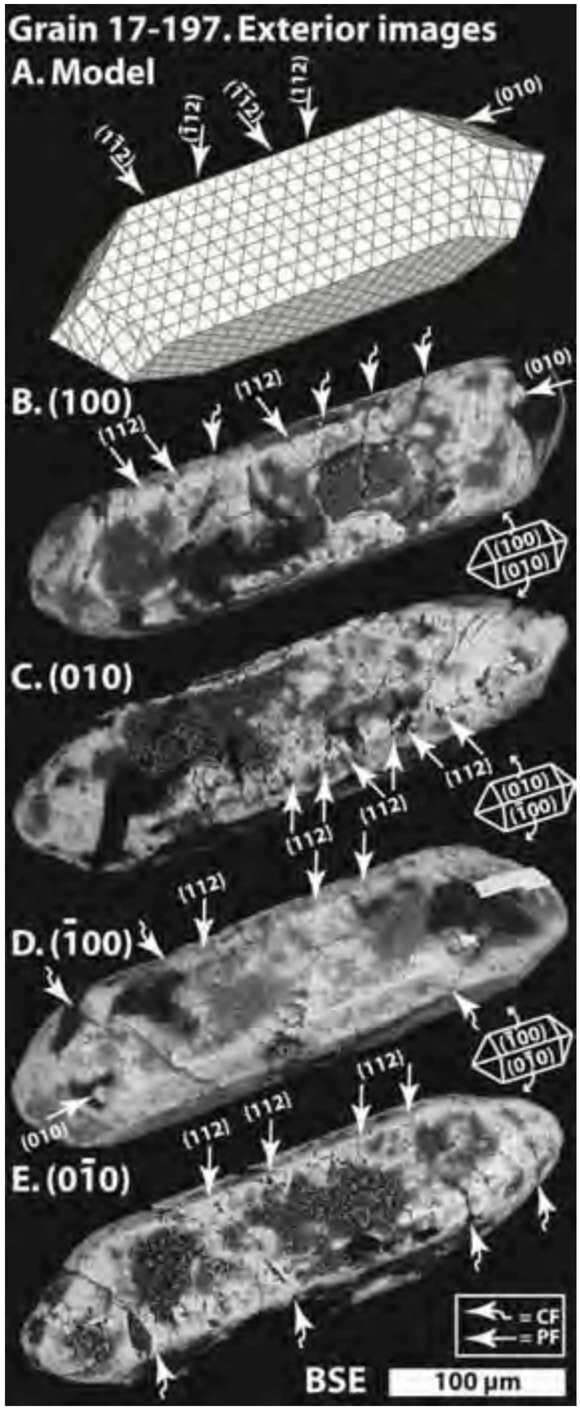
Grain 17-197. Exterior images
A. Model
B. (100)
C. (010)
D. ($\bar{1}$00)
E. (0$\bar{1}$0)
= CF
= PF
BSE
100 μm

Figure 6

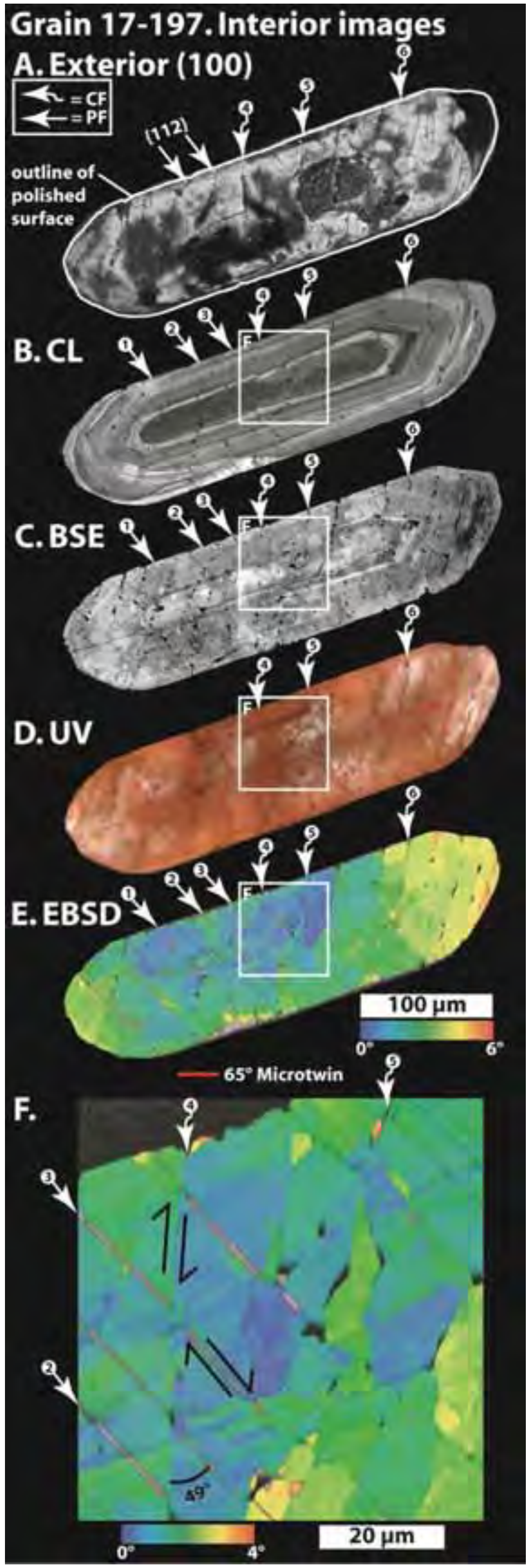
Grain 17-197. Interior images
A. Exterior (100)
= CF
= PF
(112)
outline of polished surface
B. CL
C. BSE
D. UV
E. EBSD
100 µm
0°
6°
65° Microtwin
F.
49°
0°
4°
20 µm

Figure 7

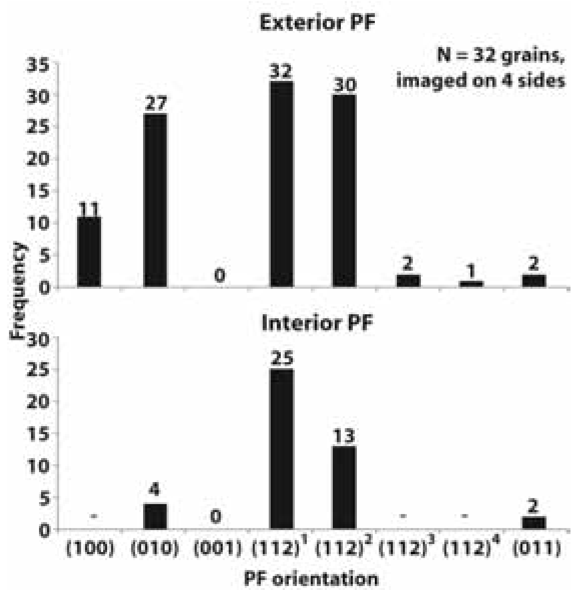
Exterior PF
N = 32 grains, imaged on 4 sides
35
30
25
20
15
10
5
0
11
27
0
32
30
2
1
2
Frequency
Interior PF
30
25
20
15
10
5
0
-
4
0
25
13
-
-
2
(100) (010) (001) (112)¹ (112)² (112)³ (112)⁴ (011)
PF orientation

Figure 8

Table 1. EBSD analysis conditions

SEM Model	Hitachi SU6600						
Grain	Grain17-158	Grain17-158 z1	Grain17-158 z2	Grain17-197	Grain17-197 z1	Grain42-1-213	Grain42-1-213 z1
Figure	5d	5f	5e	7e	7f	3d	3e
EBSP collection time per frame (ms)	17	17	17	17	17	17	17
Background (frames)	64	64	64	64	64	64	64
EBSP noise reduction (frames)	7	7	7	7	7	7	7
Binning	4x4	4x4	4x4	4x4	4x4	4x4	4x4
Gain	High	High	High	High	High	High	High
Hough resolution	60	60	60	60	60	60	60
Band detection min/max	5/7	5/7	5/7	5/7	5/7	5/7	5/7
Mean band contrast (zircon)	142.7	141.9	146.4	140.7	135.5	144.9	147.8
X steps	700	418	266	876	649	789	362
Y steps	592	325	455	512	678	447	307
Step distance (nm)	550	125	150	375	100	400	100
Average mean angular deviation (zircon)	0.3653	0.4393	0.3549	0.4108	0.4141	0.4701	0.4485
Noise reduction – 'wildspike'	No	No	No	No	No	No	No
n neighbour zero solution extrapolation	0	0	0	0	0	0	0
Kuwahara Filter	-	-	-	-	-	-	-
Hitachi SU6600 FEG-SEM settings							
EBSD system	Nordlys Detector - HKL Channel 5 SP9						
Carbon coat (<5nm)	Yes	Yes	Yes	Yes	Yes	Yes	Yes
Acc. Voltage (kV)	20	20	20	20	20	20	20
Working distance (mm)	19	19	19	19	19	19	19
Tilt (degrees)	70	70	70	70	70	70	70

Note: EBSD, electron backscatter diffraction; EBSP, electron backscatter diffraction patterns; FEG-SEM, field emission gun - scanning electron microscope.